Research Square

Preprints are preliminary reports that have not undergone peer review.
They should not be considered conclusive, used to inform clinical practice,
or referenced by the media as validated information.

Mesoporous curvature-induced proton coupled electron transfer for rapid photoredox of CO2 to CH4

Dongyuan Zhao

dyzhao@fudan.edu.cn

Fudan University https://orcid.org/0000-0001-8440-6902

Jie Zhang

Fudan University

Cong Liu

East China University of Science and Technology

Tong Wang

Fudan University

Liangliang Liu

Lanzhou University

Qing Zhang

ShanghaiTech University https://orcid.org/0000-0001-8822-1753

Xiaoming Cao

Shanghai Jiao Tong University https://orcid.org/0000-0002-4782-853X

Yun Tang

Fudan University https://orcid.org/0000-0002-2999-9626

Article

Keywords:

Posted Date: November 12th, 2026

DOI: https://doi.org/10.21203/rs.3.rs-10399019/v1

License: This work is licensed under a Creative Commons Attribution 4.0 International License.
Read Full License

Additional Declarations: There is **NO** Competing Interest.

Abstract

The photoreduction of CO_2 is usually terminated by two-electron processes resulting in predominantly products CO, the formulation of eight-electron products CH_4 still remains a great challenge limited by proton coupled electron transfer (PCET) abilities. Here, a novel type of two-dimensional (2-D) mesoporous TiO_2 ($mTiO_2$) has been synthesized based on the nanoscale titanium-oxo cluster units for rapid photoredox of CO_2 to CH_4. In this unique 2-D structure, a mesoporous sheet with ~ 2.7 nm in thickness and several micrometers in size, can be stably formed into uniform hexagonal arrays. The size of the mesopores can be precisely controlled from 8.0 to 18.0 nm by utilizing the amphiphilic di-block copolymer poly(styrene-*block*-acrylic acid) (PS-*b*-PAA) micelles with tunable block lengths. With a curvature-governed Ti^{3+} density, such mesoporous sheets demonstrate excellent photocatalytic CO_2 reduction capability by accelerating the PCET processes, achieving a record-high CH_4 production rate of 0.49 mmol g^{-1} h^{-1} with near-unique selectivity up to 99.6% under full-spectrum solar irradiation, without sacrificial reagents and co-catalysts, and the 2-D $mTiO_2$ can retain their photocatalytic activity after five consecutive cycles. An equivariant geometric deep learning model was constructed to simulate the spin density of mesoporous TiO_2, with the objective of identifying exposed active sites. Synchrotron X-ray absorption spectroscopy combined with EELS characterizations unambiguously verify that curved mesoporous interfaces induce reduced Ti – O coordination, concentrated oxygen vacancies and abundant low-valent Ti^{3+} sites while retaining the anatase crystalline phase. Density functional theory (DFT) calculations confirm that curvature-enriched Ti^{3+} sites can accelerate Volmer step and promote preferential hydrogenation to the carbon atom rather than oxygen (0.73 eV vs. 2.05 eV) due to a bent configuration of the Ti – O–Ti linkage. This atomic-scale selectivity suppresses CO formation and drives the reaction exclusively toward CH_4, establishing a direct link between mesoporous curvature and multi-electron and proton coupling pathways. This work demonstrates that efficient and selective photocatalytic process can be achived by constructing rich Ti^{3+} 2-D mesoporous structure *via* nanocluster assembly.

Introduction

The photocatalytic conversion of CO_2 into valuable fuels such as CH_4 has emerged as one of the most promising approaches for mitigating atmospheric CO_2 concentrations[1–7]. The photoreduction of CO_2 usually undergoes proton coupled electron transfer (PCET) reaction pathways that may be terminated by multi electrons (2, 4, 6, or 8 e^-) and corresponding protons coupled processes. Therefore, the formulation of products performance and selectivity has always been challenging, especially for eight electrons and protons reaction of CO_2 to CH_4[8, 9]. Traditionally, it is believed that the generated protons and photoexcited electrons are separately transported to the adsorbed CO_2 molecule[10]. Hydrogenation at different sites on the CO_2 molecule may lead to the formation of distinct products, and the unbalanced proton and electron regions on the reduction active sites may also lead to the low selectivity of target

products[11]. PCET is considered an essential model, involving the electron transfer step followed by or concerted with the instantaneous proton-transfer process[12]. Previous studies have suggested that, in the first hydrogenation step of CO_2, hydride-like species generated via the Volmer step ($H_2O + * + e^- \rightarrow *H + OH^-$) in the neutral and alkaline solution tend to be hydrogenated on the C end of CO_2 for the formation of *HCOO, while the proton preferentially facilitates the formation of *COOH[13,14]. Thus, the enhanced *HCOO formation could suppress the competing *COOH pathway, thereby disfavoring CO formation[15]. Therefore, accelerating the Volmer step is crucial for supplying active hydride-like *H species for the high CH_4 selectivity of CO_2 hydrogenation. Furthermore, since the Volmer step itself is a PCET process and the PCET process is also critical for the subsequent stepwise hydrogenation from *HCOO, accelerating the PCET process could promote CH_4 produciton. Despite efforts to enhance CO_2 conversion into CH_4 through the strategies such as energy band-gap engineering[16], surface vacancy engineering[17], crystal facet engineering[18], micro/nano engineering[19], cocatalysts engineering[20], interfacial engineering (hetero-junction and Z-scheme system)[21], precious metal alloying[22], and Cu species modulation[23–25] by accelerate PCET, photocatalysts designed to substantially improve both selectivity and performance are lacking. Therefore, the elaborate design of the photocatalyst nanostructures to facilitate the key Volmer step and PCET for continuous production of multi electron and proton products at the active site is essential for highly selective conversion of CO_2 to CH_4.

Two-dimensional (2-D) materials, featuring high exposed active sites, large surface area, unique optical and electrical properties, are highly desirable for constructing photocatalytic system[26–29]. 2-D materials can provide much defects as trapping sites for photo-generated charges capture, promote charges separation, migration, and collection, thus facilitate the photocatalytic PCET process[30–32]. A typical PCET photoredox reaction of CO_2 to CH_4 primarily comprises photo-absorption, electron-hole separation, CO_2 reduction by photo-excited electrons, and protons-electrons coupling (hydrogenation); the first two-steps are closely related to the conversion efficiency, while the last two-steps mainly determines the final product selectivity[24]. To realize efficient electron-hole separation, it is necessary to design defective semiconductors, because the defect sites may act as trapping caves to capture photo-excited electrons or holes, hence enabling carrier separation[33]. The reduction pathway generally includes the adsorption and activation of CO_2, and the C – O bond dissociation. The ultimate product selectivity critically depends on the relative energy levels of the reactive intermediates[34]. The selection of semiconductors, such as titanium dioxide (TiO_2), should prioritize those with optimal electronic properties, including high electron density and abundant active sites, to facilitate efficient PCET reactions, especially for the Volmer step towards CH_4 production.

Recently, the introduction of oxygen vacancies has provided a powerful method to manipulation PCET process and enhance the performance of CO_2 photo-conversion[35–37]. For instance, the introduction of oxygen vacancy defects into TiO_2 surface can effectively control the electronic structure, promote the charge transfer ability, give rise to highly enhanced photoredox[38]. Moreover, these vacancies often

generate trivalent titanium (Ti^{3+}) species, which further contribute to electron enrichment and provide abundant active sites for CO_2 photoreduction. To maximize the benefits of oxygen vacancies, a material architecture that can stabilize a high density of such defects is highly desirable. In this regard, functional mesoporous materials are endowed with standalone nanosized spaces, high surface areas and large pore volumes[39, 40]. Notably, their curved pore surfaces can induce strain, which is particularly effective for creating and stabilizing enriched oxygen vacancies, exhibiting potentials in realizing the photocatalytic conversion CO_2 to CH_4[9]. Therefore, the integration of oxygen vacancy and enhancement of Ti^{3+} species into 2-D oriented mesoscopic TiO_2 nanostructure holds the potential to yield a highly promising photocatalyst, one that combines multiple advantages and is poised to further unlock the full potential of photocatalysis in PCET process[41, 42]. The controlled synthesis of ordered mesoporous architectures offers a promising route to enhance photocatalytic performance. However, conventional approaches rely on molecular precursors like tetrabutyl orthotitanate (TBOT), which typically fail to precisely couple mesoporous curvature with atomic-scale defect engineering, particularly for stabilizing catalytically active sites like Ti^{3+}. Moreover, the mechanistic role of mesopore curvature in directing multi-electron reaction pathways, such as the critical PCET steps in CO_2-to-CH_4 conversion, remains poorly understood, limiting the rational design of selective photocatalysts.

Herein, 2-D mesoporous TiO_2 nanosheets (2-D mTiO_2) with a high Ti^{3+} content at mesoporous curvature surface have been successfully fabricated by the novel salt-templated cluster-micelle co-assembly (ST-CMCA) approach: the co-assembly of block copolymers poly(styrene-*block*-acrylic acid) (PS-*b*-PAA) with titanium-oxo cluster (TOCs) precursors under sodium chloride (NaCl) crystal templates. The resultant sheet-like structures exhibit remarkable mechanical properties, being able to extend to several micrometers without fracture, with a uniform thickness of 2.7 nm. Furthermore, the 2-D mTiO possesses a large pore size of approximately 11.7 nm, featuring a high surface area of ~ 136 $m^2\ g^{-1}$. And the mesopore sizes can be adjusted ranging from 8.0 to 18.0 nm. Ultimately, the obtained 2-D mesoporous structure demonstrates exceptional PCET ability and photocatalytic CO_2 reduction capability, achieving a CH_4 production rate of 0.49 mmol $g^{-1}\ h^{-1}$ and an impressive selectivity for CH_4 up to 99.6% under full-spectrum solar irradiation, without sacrificial reagents and co-catalysts, ranking among the highest values reported to date for pure TiO_2-based photocatalysts, and the 2-D mTiO_2 retain their photocatalytic activity after five consecutive cycles. Furthermore, the mesoporous curvature, which governs the Ti^{3+} density of 2-D mTiO_2, can induce the PCET pathways and further enable to drive the photoredox of CO_2 to CH_4. The established equivariant geometric deep learning model for the simulation of mesoporous TiO_2 spin density validates the enrichment of the exposed Ti^{3+} sites by the curvature, contributing to protons and electrons transfer process in photoredox. Density functional theory (DFT) calculations confirm that the curvature-enriched Ti^{3+} sites and the bent configuration of Ti – O–Ti linkage in the mesoporous TiO_2 significantly enhance the Volmer step, enabling efficient *H supply for CO_2 activation and steering the reaction toward the *HCOO intermediate, which suppresses CO formation and drives the reaction exclusively toward CH_4 (0.73 eV vs. 2.05 eV). Deep learning and DFT calculations proved

that the mesoporous curvature induced Ti^{3+} sites directly contribute to the enhanced photoredox performance for CO_2 to CH_4.

Results

Synthesis and characterization of 2-D mTiO_2

2-D mTiO_2 can be synthesized through the salt-templated cluster-micelle co-assembly (ST-CMCA) approach spatially confined on salt NaCl crystal templates by tailoring interactions between TOCs ($Ti_{32}O_{16}$, $Ti_{32}(\mu_2\text{-}O)_8(\mu_3\text{-}O)_8(OCH_2CH_2O)_{32}(C_4H_9COO)_{16}$ $(OCH_2CH_2OH)_{16}$) and the diblock copolymer of PS-*b*-PAA micelles to mediate the formation of the 2-D mesoporous architecture (Fig. 1). Optical images show that the TOCs building blocks, are colorless crystalline materials and can be soluble in dichloromethane (Figure S1 and S2). As shown in the field-emission scanning electron microscopy (FESEM) images (Fig. 2a), the 2-D mTiO_2 slices in well-retained morphology are random stacked. The uniform 2-D mTiO_2 are composed of slightly curved slices with several micrometers in length and several micrometers in width (Fig. 2a). The ordered large mesopores in the 2-D mTiO_2 can be observed (Fig. 2b). The transmission electron microscopy (TEM) images reveal a mesoporous structure with hexagonal arrangement (Fig. 2c). The atomic force microscopy (AFM) tomography (Fig. 2d) and thickness analysis (Fig. 2d inset) disclose that the similar 2-D mesoporous morphology and structure to that of the SEM and TEM images. The AFM measurements further show that the 2-D mTiO_2 samples have rough surfaces with an approximate thickness of 2.7 nm.

The TEM images reveal that the mesopore size is ~ 11.7 nm (Figure S3 and S4), and further show that the periphery of the mesoporous structures exhibit a significant amount of lattice fringes. The high-resolution TEM (HR-TEM) images point out that the parallel lattice fringes with consistent orientations over the entire image region along with an interplanar spacing of 0.35 nm, which corresponds to the (101) plane of anatase TiO_2 (Figure S4 a, b and c). Atomic-resolution high-angle annular dark-field scanning transmission electron microscopy (AC-HAADF-STEM) image displays well-ordered atomic lattices for crystalline anatase 2-D mTiO_2 without obvious structural distortion (Fig. 2e). The X-ray diffraction (XRD) pattern shows well-defined diffraction peaks at 25.5, 37.8, 48.0, 53.8, 55.2, and 62.9°, which can be indexed to the 101, 004, 200, 105, 211, and 214 reflections of anatase, demonstrating the highly crystallized anatase phase (space group $I4_1/amd$) of the 2-D mTiO_2 (Fig. 2f). The selected-area electronic diffraction (SAED) pattern displays well-resolved diffraction rings and numerous spots (the inset of Figure S3), further indicating a crystallized anatase nanosheets. Energy dispersive spectrometer (EDS) mapping images disclose that a pure and homogeneous distribution of the Ti and O elements in the whole materials (Figure S4d). Raman spectra show typical bands at 143, 238, and 437 cm^{-1} which can be attributed to vibrational bands of E_g, $B_{1g,}$ and A_{1g} for anatase phase (Fig. 2g)[35], congruent with the XRD data.

The nitrogen adsorption-desorption isotherms of the 2-D $mTiO_2$ exhibit the characteristics of type IV according to the classification of the International Union of Pure and Applied Chemistry (IUPAC). The hysteresis loop at a high relative pressure ($0.6 < P/P_0 < 1.0$) indicates the presence of mesopores (Fig. 2h). The Brunauer-Emmett-Teller (BET) surface area and total pore volume of the 2-D $mTiO_2$ are calculated to be as large as ~136 $m^2 g^{-1}$ and ~0.33 $cm^3 g^{-1}$, respectively. The pore size distribution based on the Barrett-Joyner-Halenda (BJH) model is centered at ~ 11.7 nm (Fig. 2i), which is conciconse with TEM results.

The Fourier-transform infrared (FTIR) spectra reveal an obvious band at around 3400 cm^{-1}, which is attributed to the vibration of hydroxy groups (Figure S5a). The X-ray photoelectron spectroscopy (XPS) surveys of the 2-D $mTiO_2$ (Figure S5b) prove the coexistence of Ti and O elements without any other impure elements. The Ti 2p XPS spectrum (Figure S5c) depicts two bands at 464.9 eV (Ti $2p_{1/2}$) and 458.9 eV (Ti $2p_{3/2}$), corresponding to the Ti^{4+} oxidation states. The Ti 2p XPS spectrum of O 1s shows two distinct chemical states. The sharp band at 530.2 eV and the broad band at 532.1 eV can be assigned to O − Ti and O − H bonds, respectively (Figure S5d), indicating the presence of rich Ti − OH groups on the surface of the 2-D $mTiO_2$[43].

X-ray absorption near-edge structure (XANES) measurement shows that the similarity in XANES features between 2-D $mTiO_2$ and TiO_2 implies that TiO_2 remain as the anatase phase after mesopore introducing (Fig. 3a). It also shows that the absorption edge of 2-D $mTiO_2$ shifts to lower energy compared to that of TiO_2, which indicates partial Ti atoms are reduced during mesopore information process. Fourier Transform extended X-ray absorption fine structure (FT-EXAFS) clearly shows the reduced Ti-O coordination number after mesopore information, indicating the appearance of oxygen vacancies (Fig. 3b). Wavelet transform EXAFS (WT-EXAFS) shows that Ti in 2-D $mTiO_2$ has similar local structure as that in TiO_2, with a weakened scattering peak locating at k ~ 6 $Å^{-1}$ and R ~ 1.5 Å corresponding to reduced Ti-O coordination number (Fig. 3c). Ti L-edge electron energy loss spectroscopy (EELS) reveals stronger signal intensity at curved interfaces, corresponding to abundant low-valent Ti sites (Fig. 3d). The HAADF-STEM (Fig. 3e) distinguishes linear grain boundaries and curved pore interfaces (I, II, III, IV were selected for EELS analysis). Quantitative normalized O K-edge intensities (Fig. 3f) further verify the decreased oxygen content at curved pore walls, unambiguously confirming the concentrated oxygen vacancies at the curved mesopore interfaces.

Formation process of the 2-D mTiO

The formation of the 2-D $mTiO_2$ mainly undergoes four steps: the formation of composite micelles, direct assembly on the surface of NaCl crystals, calcination and water washing (Fig. 1). Typically, cyclic TOCs precursors with a permanent microporosity are used as the building units, which can be prepared according to the work reported previously[44]. First, these clusters can be dissolved in dichloromethane to form a well-dispersed cluster solution (Figure S2, left). Then, the amphiphilic di-block copolymer of PS-*b*-

PAA is added to form a pale blue solution of PS-*b*-PAA/TOCs composite micelles, which exhibits an obvious Tyndall effect (Figure S2, right). Afterwards, these composite micelles are co-assembled to generate a uniform hexagonal transparent film during the solvent evaporation processes. Subsequently, the mesoporous TiO_2 with salt NaCl can be obtained after removing the micelle templates by the calcination in nitrogen (N_2) and air, respectively. Finally, the 2-D mesoporous TiO_2 nanosheets can be obtained by removing the salt template by water washing (Fig. 1).

A precursor solution containing TOCs/PS-*b*-PAA composite micelles (Figure S6) was introduced into a glass column packed with micron-sized NaCl crystals of cubic morphology (Figure S7). Following vacuum filtration to remove excess solution, a thin liquid film of the precursor remained coated on the crystal surfaces. After the evaporation at room temperature for 12 hours, this film formed a uniform monolayer coating (Figure S8). The FESEM images confirm the formation of a 2-D monolayer structure on the NaCl templates after the 12-hour evaporation (Figure S8). Further FESEM analysis reveals that the TOCs/PS-*b*-PAA composites undergo the solvent evaporation and solidification, resulting in well-defined 2-D nanosheets (Figure S9). The EDS mapping demonstrates a pure and homogeneous distribution of Ti and O elements throughout the sample (Figure S10). As shown in FESEM images, the subsequent calcination of this structure successfully yielded 2-D mesoporous TiO_2 ($mTiO_2$ periphery, Figure S11 and 12).

Precise control over mesoporous curvature

The mesopores curvature of the 2-D $mTiO_2$ products can be precisely engineered by tailoring their pore size, which is controlled by varying the block lengths of the lab-made amphiphilic PS-*b*-PAA copolymers (Fig. 13,Table S1). FESEM images confirm that all of these samples derived from PS-*b*-PAA with different segment lengths retain a well-retained 2-D morphology and mesoporous architecture (Fig. 13a, d and g). The TEM analysis further demonstrates that the average pore size of the 2-D $mTiO_2$ can be controllably adjusted, with measured values of 8.0 ± 2.0 (2-D $mTiO_2$-8.0 by PS_{12000}-*b*-PAA_{1100}, Fig. 3b), 13.0 ± 1.8 (2-D $mTiO_2$-13.0 by PS_{13000}-*b*-PAA_{1200}, Fig. 13e) to 18.0 ± 2.7 nm (2-D $mTiO_2$-18.0 by PS_{15000}-*b*-PAA_{4800}, Fig. 13h), respectively.

The 2-D $mTiO_2$ samples with different pore diameters all exhibit type IV nitrogen adsorption-desorption isotherms, with hysteresis loops in the high relative pressure region ($0.6 < P/P_0 < 1.0$) confirming their mesoporous nature (Figure S14)[43]. The BET surface areas were determined to be ~148 $m^2\ g^{-1}$ (2-D $mTiO_2$-8.0), ~130 $m^2\ g^{-1}$ (2-D $mTiO_2$-13.0), and ~112 $m^2\ g^{-1}$ (2-D $mTiO_2$-18.0), with BJH pore size distributions centered at ~8.0, 13.0, and 18.0 nm, respectively (Fig. 13c, f, i). The XRD patterns confirm the anatase phase, showing characteristic diffraction peaks at 25.5, 37.8, 48.0, 53.8, 55.2, and 62.9º, respectively (Figure S15, left). Raman spectra show typical bands at 143 cm^{-1} (E_g), 238 cm^{-1} (B_{1g}), and 437 cm^{-1} (A_{1g}) for anatase phase, congruent with the XRD data (Figure S15, right).

Photocatalytic CO reduction

The UV-Vis diffuse reflectance spectra (Fig. 4a) reveal that the 2-D mTiO_2 samples exhibit a notable red-shifted absorption and enhanced light harvesting across the 400–600 nm range compared to the P25 benchmark, indicative of a broader spectral response. The band gaps (E_g) of the 2-D mTiO_2 and commercial P25 are calculated to be 2.90 and 2.96 eV, respectively (Figure S16). The electrochemical impedance spectra (Fig. 4b) show that the 2-D mTiO_2 exhibit a smaller arc radius compared to that of the commercial P25, indicating that the interfacial electron-transfer resistance in the 2-D mTiO_2 is much smaller than that in P25. The photoelectrochemical (PEC) measurements show that the 2-D mTiO_2 samples exhibit a higher photo-response. The photocurrent intensity of the 2-D mTiO_2 is nearly 6 times higher than that of P25, suggesting the apparently enhanced charge separation compared with P25 (Fig. 4c). The charge dynamics of the 2-D mesoporous structures were investigated by surface photovoltage (SPV) spectra. The 2-D mTiO_2 show a SPV peak of 0.014 mV at ~ 330 nm, much higher than those of P25 (0.001 mV), indicating that the density of surface-accumulated holes significantly decreases.

The 2-D mTiO_2 nanosheets demonstrate markedly enhanced photocatalytic CO_2 reduction performance under solar irradiation (Fig. 4), outperforming mesoporous TiO_2 spheres (mTiO_2 sphere, Figure S17), bulky mesoporous TiO_2 nanocrystals (mTiO_2 nanocrystal, Figure S18 and S19), and commercial P25. Particularly, the CH_4 production rate over 2-D mTiO_2 is substantially higher than those of all control samples over a 4 hour period (Fig. 4e).

The 2-D mTiO_2 products exhibit the best performance with CH_4 evolution rates of 0.49 mmol g^{-1} h^{-1}, which is 1.9 times higher than that of mTiO_2 sphere (0.26 mmol g^{-1} h^{-1}), 1.6 times higher than that of mTiO_2 nanocrystal (0.32 mmol g^{-1} h^{-1}), 14.5 times higher than that of the P25 (0.03 mmol g^{-1} h^{-1}) (Fig. 4e). Additionally, after repeating the photocatalytic CO_2 reduction experiments for 5 times, the 2-D mTiO_2 nanosheets exhibit consistent photoactivity as the initial circle, with no apparent decay (Fig. 4f). The TEM images reveal that the unique mesoporous architecture is well-preserved after the long-term cycles, suggesting the excellent photostability (Figure S20). The 2-D mTiO_2 nanosheets show an ultra-high 99.6% (near 100%) selectivity for CH_4, ranking among the highest values reported to date for pure TiO_2-based photocatalysts (Figure S21 and Table S2). Additionally, the 2-D mTiO_2 also exhibit much higher CH_4 generation rates of up to 117.7 μmol g^{-1} h^{-1} under the visible light region, far exceeding that of mTiO_2 sphere (4.48 μmol g^{-1} h^{-1}), mTiO_2 nanocrystal (89.62 μmol g^{-1} h^{-1}), and commercial P25 (0.89 μmol g^{-1} h^{-1}) (Figure S22). The CH_4 yield of 2-D mTiO_2 nanosheets exceeds those of all reference catalysts under both simulated sunlight and visible-light irradiation (Fig. 4g). The 2-D mTiO_2 sample can be achieved a quantum efficiency (QE) of 4.54% for the photocatalytic reaction (Figure S23). The photoluminescence (PL) spectrum of the 2-D mTiO_2 exhibits a distinct band similar to that of the P25, but with a significantly decreased intensity (Figure S24), indicating the apparently reduced

recombination of the charge carriers. The Kelvin probe force microscopy (KPFM) shows that the 2-D mTiO_2 nanosheets exhibit a distinct rise after a light irradiation, indicating the electron excitation to the conduction band in the mesoporous semiconductor on the surface (Figure S25).

The sample of 2-D mTiO_2-13.0 delivers the highest CH_4 evolution rate (0.49 mmol g^{-1} h^{-1}), surpassing both 2-D mTiO_2-13.0 and 2-D mTiO_2-13.0 (both 0.44 mmol g^{-1} h^{-1}) (Fig. 4h, i and S26). While all three samples exhibit strong and broad light absorption in the 300–600 nm range (Figure S27) and comparable CO_2 uptake capacities (Figure S28), PEC measurements reveal a clear differentiation: 2-D mTiO_2-13.0 generates the highest photocurrent density among the series (Figure S29), indicating its superior charge-carrier separation efficiency. This optimized photoelectrochemical response aligns directly with its peak catalytic activity, suggesting that the specific curvature associated with ~ 13 nm pores most effectively promotes the separation and utilization of photogenerated charges.The contact angle of water droplets on the deposited film based from the mesoporous TiO_2 solution are 37º, 30.1º and 33.1º for 2-D mTiO_2-8.0, 2-D mTiO_2-13.0 and 2-D mTiO_2-18.0, respectively, due to their hydrophilic groups (Figure S30). The electron paramagnetic resonance (EPR) spectra reveal distinct characteristic signals of the TEMPO spin probe. In the presence of mesoporous TiO_2, the intensity of these TEMPO signals decreases under light irradiation, indicating that a greater number of photoexcited electrons are transferred from the mesoporous TiO_2 to the TEMPO acceptor (Figure S31, S32, S33). It also proves that the 2-D mTiO_2 nanosheets can generate more electrons through the light irradiation when compared to that in the dark. The band intensity of the EPR spectra for the 2-D mTiO_2-13.0 is lower than that of the 2-D mTiO_2-8.0 and 2-D mTiO_2-18.0, indicating that the former can generate more electrons compared under a light irradiation (Figure S34).

The Ti^{3+} density in the 2-D mTiO_2 nanosheets with different pore sizes were predicted by equivariant geometric deep learning model (Figure S35). Three TiO_2 mesoporous structure models with the pore diameters of 8.0 nm (2-D mTiO_2-8.0), 13 nm (2-D mTiO_2-13.0), and 18 nm (2-D mTiO_2-18.0), were constructed, respectively. For TiO_2, spin density is absent for Ti^{4+} due to its fully paired electrons; in contrast, Ti^{3+} exhibits nonzero spin density as a direct consequence of its single unpaired electron. (Figure S35)[45, 46]. Within the internal surface of the mesopore, the 2-D mTiO_2-13.0 exhibits the highest Ti^{3+} density, while 2-D mTiO_2-8.0 exhibits the lowest Ti^{3+} density (Fig. 5a, left). In terms of Ti^{3+} species evaluation, the XPS spectra of elemental Ti were provided. Two bands at 465.1 eV ($Ti_{2p1/2}$ assigned to Ti^{4+}) and 459.2 eV ($Ti_{2p3/2}$) can be states (Figure S36a). The positive band shift of $Ti_{2p3/2}$ with different pore sizes implies the existence of Ti^{3+} species. The EPR spectra (Figure S36b) show strong *g*-value of 2.0, confirming the presence of oxygen vacancy, concomitant with Ti^{3+} species. The 2-D mTiO_2-13.0 has the highest EPR response compared to 2-D mTiO_2-8.0 and 2-D mTiO_2-18.0, confirming the highest Ti^{3+} density of 2-D mTiO_2-13.0 (Fig. 5a, right).

The *In-situ* FT-IR spectroscopy of 2-D mTiO_2 shows that the emergences of bands at approximately 1432, 1319 and 1369 cm^{-1} are assigned to bidentate carbonate (HCO_3^-, 1432 cm^{-1}), monodentate carbonate (*m*-CO_3^{2-}), and bidentate carbonate (*b*-CO_3^{2-}, 1369 cm^{-1}) species, respectively, confirming CO_2 adsorption onto the photocatalyst surface. Furthermore, the detection of the *HCOO intermediate at about 1585 cm^{-1} supports its role as a critical intermediate in the pathway toward carbon-containing products (Fig. 5b and S37a)[21, 24]. Conversely, the *In-situ* FT-IR spectroscopy of commercial P25 shows that the emergences of negative absorbance bands at approximately 1655 cm^{-1} are assigned to unstable *COOH intermediates (Fig. 5c and S37b). The generated *COOH species rapidly decompose and desorb instead of accumulating on the surface. Importantly, no obvious growing absorption signal assigned to *HCOO can be identified over P25. Moreover, the intensities of carbonate species and deep hydrogenation intermediates are markedly weaker compared with 2D mTiO_2, as also evidenced by the contour map, demonstrating inferior CO_2 activation capacity and blocked deep hydrogenation pathways.

Discussion

Oxygen vacancies and Ti^{3+} in these 2-D mTiO_2 nanosheets are created by the mesopore curvature, which can be regulated by mesopore sizes. This defect introduces a localized charge imbalance. To compensate for the charge imbalance caused by the oxygen vacancy, no spin density Ti^{4+} at the oxygen vacancy is reduced to Ti^{3+} [47, 48]. The Ti^{3+} sites play a crucial role in the CO_2 photoreduction reaction. First, on the one hand, the electrons trapped in the Ti^{3+} sites can facilitate the CO_2 reduction by being transferred to the CO_2 molecules, directly helping to break the C = O double bonds[49, 50]. On the other hand, the electrons could enhance the Volmer step in the neutral or alkaline aqueous solution for *H formation, thereby accelerating hydrogen-assisted CO_2 activation. Second, when the Ti^{3+} site loses electrons and is oxidized to Ti^{4+}, it can act as an electron trap[51–54]. When TiO_2 absorbs light, electrons are excited from the valence band to the conduction band, leaving behind holes. The coordinative unsaturation of Ti^{3+} sites enables them to trap and localize electrons[52, 53]. This helps in localizing and stabilizing the electrons, preventing them from recombining with the holes in the valence bands. This stabilization of electrons is essential for the reduction half-reaction. It is found that unstable lattice oxygen and oxygen vacancies are easily generated at high curvatures due to the localized lattice strain[55]. However, it is worth noting that Ti^{3+} density does not simply increase linearly with increasing curvatures in our work. Because during the stabilization of the mesoporous structure, stress release could occur, leading to a reduction in local stresses. This process may result in a relative decrease in the formation of oxygen vacancies, as atomic arrangements tend to stabilize, which in turn reduces the amount of Ti^{3+}. The Lindemann indices for the geometry optimization of 2-D mTiO_2-8.0, 2-D mTiO_2-13.0, and 2-D mTiO_2-18.0 were calculated to be 0.011, 0.004, and 0.004, respectively[56]. The higher Lindemann index indicates that 2-D mTiO_2-8.0 tends to undergo more significant structural relaxation to stabilize the mesopore, suggesting greater stress release. This may account for the lower Ti^{3+} density observed in 2-D mTiO_2-

8.0. In contrast, the smaller structural changes in 2-D mTiO_2-13.0 and 2-D m TiO_2-18.0 correspond to a higher Ti^{3+} density. This curvature-dependent defect enrichment behavior is fully validated by atomic-level synchrotron and electron spectroscopy characterizations. XANES spectra confirm the preserved anatase framework of 2D mTiO_2 with a shifted absorption edge indicative of partial Ti reduction, while FT-EXAFS and WT-EXAFS reveal declined Ti – O coordination numbers originating from curvature-triggered lattice strain and oxygen vacancy generation. HAADF-STEM combined with Ti L-edge and O K-edge EELS further directly visualizes that oxygen vacancies and Ti^{3+} species are selectively concentrated on curved pore walls instead of flat grain boundaries, offering solid evidence that mesoporous curvature serves as a structural regulator to spatially regulate the density of catalytically active Ti^{3+} sites. Time-resolved in-situ FTIR measurements further provide direct spectroscopic evidence for pathway switching, revealing distinct intermediate evolution behaviors between curved 2D mTiO_2 and linear commercial TiO_2.

To elucidate the underlying mechanisms responsible for high productivity and selectivity, DFT was employed to construct viable pathways for CO_2 reduction (Fig. 5d). For the CO_2 reduction reaction simulation, a representative segment of the pore structure with a pore diameter of 13.0 nm was selected. H_2O dissociation was first calculated on the pore structured model. In contrast to the strongly endergonicity of Volmer step at Ti sites on the mainly exposed anatase TiO_2 (101) surface in conventional TiO_2 such as P25, the curved surface of mesoporous TiO_2 enables the Volmer step to be exergonic (Figure S38 and S39). This indicates that the Volmer step could occur in the 2-D mTiO_2-13.0. Meanwhile, the proton transfer from water to the lattice oxygen ($H_2O + O_{lat} \rightarrow HO_{lat}^- + OH^-$) is also thermodynamically favorable. As illustrated in the free energy pathway (Fig. 5d), the chemisorbed *H at the Ti^{3+} sites by the enhanced Volmer step renders the CO_2 activation to undergo the hydrogen-assisted pathways initiating from the hydrogenation either at the oxygen end (CO_2 + *H → *COOH), or at the carbon end (CO_2 + *H → *HCOOH). The free energy of activation for *HCOO formation ($\Delta G^{\ddagger}$ = 0.73 eV) is substantially lower than that for *COOH formation ($\Delta G^{\ddagger}$ = 2.05 eV). Consequently, the reaction preferentially proceeds *via* the *HCOO pathway, effectively suppressing further hydrogenation of *COOH to CO (Figure S40). As the *H at the Ti^{3+} site is consumed, the subsequent stepwise hydrogenation would occur through the PCET process with the proton from the neighboring lattice oxygen site. The hydrogenation of *HCOO to *HCOOH requires overcoming a barrier of 0.94 eV. The third hydrogenation step then attacks the oxygen atom distal to the surface, producing *CHO and H_2O with a modest barrier of 0.35 eV. The *CHO intermediate undergoes further hydrogenation to form *CH_2O ($\Delta G^{\ddagger}$ = 0.79 eV), which can be further hydrogenated to yield *CH_2OH ($\Delta G^{\ddagger}$ = 0.79 eV). The C – O bond cleavage in *CH_2OH proceeds with a barrier of 0.97 eV, releasing H_2O and generating the highly reactive *CH_2 species. Finally, two successive hydrogenation steps convert *CH_2 to *CH_3 ($\Delta G^{\ddagger}$ = 0.37 eV) and to CH_4 ($\Delta G^{\ddagger}$ = 0.96 eV) sequentially (Figure S41). Therefore, the mesopore curvature-induced Ti^{3+} sites not only promote the Volmer step but also steer the CO_2 hydrogenation pathway toward the C sites, which effectively

suppresses CO formation and directs the reaction cascade toward CH_4 *via* a low-barrier *HCOO route at O sites. This could be attributed to the fact that the Ti – O–Ti linkage in conventional TiO_2 such as P25 usually adopts a nearly linear geometry, where hydrogen could only be chemisorbed atop the Ti^{4+} site, while the incorporation of mesopores imposes pronounced curvature, inducing substantial bending of Ti – O–Ti bonds, shortened Ti – Ti interatomic distance, and local lattice strain. This structural distortion could promote the formation of oxygen vacancies and facilitate the emergence of a cooperative active centre comprising Ti^{3+} sites, which strongly adsorbs and enriches *H from the water (Fig. 5e). Compared to the oxophilic proton, the carbophilic *H significantly lower the obstacle of hydrogenation at the C end of CO_2 (Fig. 5f and g). Consequently, the hydrogenation target shifts from the oxygen to the carbon atom of CO_2, steering the pathway toward deep hydrogenation and ultimately enabling highly selective methane generation. Consistently, in-situ FTIR spectra confirm continuous accumulation of the key *HCOO intermediate on 2D mTiO_2, whereas unstable transient *COOH species dominate over P25 without observable *HCOO signals, perfectly corroborating the predicted reaction route divergence.

Conclusions

In summary, a novel type of unique 2-D mTiO_2 nanosheets with featuring an elevated concentration Ti^{3+} species has been successfully synthesized by the ST-CMCA approach. Such mesoporous TiO_2 nanosheets exhibit well-defined 2-D morphology with lateral dimensions of several micrometers, an ultrathin thickness of approximately 2.7 nm, and a highly defective mesopore framework rich in Ti^{3+} sites, a high surface area of $\sim$ 136.0 $m^2\ g^{-1}$, and a pore size of $\sim$ 11.7 nm. Such a mono-micelle and titanium-oxo clusters co-assembly strategy also enables the regulation of the mesopore size (8.0–18.0 nm) and curvature. A highly promoted photocatalytic CO_2 reduction with a CH_4 production rate of 0.49 mmol $g^{-1}\ h^{-1}$ and selectivity of 99.6% on full wavelength solar without sacrificial reagents and co-catalysts can be realized due to uniform 2-D structures and mesopore curvature. Notably, the mesoporous curvature change induced by pore sizes can influence the PCET capability and affect rate of photoredox. Equivariant geometric deep learning model verified that the 2-D mTiO_2-13.0 has the highest Ti^{3+} density and exposed active sites. DFT calculations confirm that curvature-enriched Ti^{3+} sites and the bent configuration of Ti – O–Ti linkages can accelerate the Volmer step, thereby promoting preferential hydrogenation to the carbon atom rather than oxygen (0.73 eV vs. 2.05 eV). This atomic-scale selectivity suppresses CO formation and drives the reaction exclusively toward CH_4, establishing a direct link between mesoporous curvature and multi-electron and proton coupling pathways. This work underscores a better insight over sophisticated clusters assembly, as well as a pathway for synthesizing 2-D mesoporous structures toward advanced energy application, demonstrated that the rational design of mesoporous curvature induced Ti^{3+} could effectively modulate the selectivity and activity of CO_2 photoreduction by manipulating the reaction pathways and optimizing key PCET steps, such as the Volmer step.

Declarations

Notes

The authors declare no competing financial interests.

Author Contributions

[#]Jie Zhang, Cong Liu, Tong Wang and LiangLiang Liu contributed equally to this work.

Acknowledgment

The authors are thankful for support from the National Key Research and Development Program of China (2023YFA1507600), the Key Basic Research Program of Science and Technology Commission of Shanghai Municipality (25PY2600100) and China National Postdoctoral Program for Innovative Talents (BX20240088), China Postdoctoral Science Foundation (2025M780902, 2024M760494).

Associated content

The Supporting Information is available free of charge.

Author information

Corresponding Authors

* Dongyuan Zhao – Laboratory of Advanced Materials, Department of Chemistry, Shanghai Key Laboratory of Molecular Catalysis and Innovative Materials, State Key Laboratory of Porous Materials for Separation and Conversion, Fudan University, Shanghai 200433, P. R. China; Shanghai Wusong Laboratory of Materials Science, Shanghai 201999, P. R. China.

Email: dyzhao@fudan.edu.cn

* Yun Tang – Laboratory of Advanced Materials, Department of Chemistry, Shanghai Key Laboratory of Molecular Catalysis and Innovative Materials, State Key Laboratory of Porous Materials for Separation and Conversion, Fudan University, Shanghai, 200433, P. R. China; Shanghai Wusong Laboratory of Materials Science, Shanghai 201999, P. R. China; SINOPEC Dalian Research Institute of Petroleum and Petrochemicals Co., Ltd., Dalian 116045, P. R. China.

Email: yuntang@fudan.edu.cn

* Xiao-Ming Cao – School of Chemistry and Chemical Engineering, Shanghai Jiao Tong University, Shanghai 200240, P. R. China

Email: xmcao@sjtu.edu.cn

Authors

Jie Zhang – Laboratory of Advanced Materials, Department of Chemistry, Shanghai Key Laboratory of Molecular Catalysis and Innovative Materials, State Key Laboratory of Porous Materials for Separation and Conversion, Fudan University, Shanghai, 200433, P. R. China;

Cong Liu –School of Chemistry and Chemical Engineering, Shanghai Jiao Tong University, Shanghai 200240, P. R. China;

Tong Wang – Laboratory of Advanced Materials, Department of Chemistry, Shanghai Key Laboratory of Molecular Catalysis and Innovative Materials, State Key Laboratory of Porous Materials for Separation and Conversion, Fudan University, Shanghai, 200433, P. R. China;

LiangLiang Liu – Key Laboratory of Nonferrous Metal Chemistry and Resources Utilization of Gansu Province, College of Chemistry and Chemical Engineering, Lanzhou University, Lanzhou 730000, P. R. China

Qing Zhang – Shanghai Key Laboratory of High-resolution Electron Microscopy, School of Physical Science and Technology, ShanghaiTech University, Shanghai 201210, P. R. China

References

1. Jiang Z, Xu X, Ma Y, Cho HS, Ding D, Wang C, Wu J, Oleynikov P, Jia M, Cheng J, Zhou Y, Terasaki O, Peng T, Zan L, Deng H (2020) Filling metal-organic framework mesopores with TiO_2 for CO_2 photoreduction. Nature 586(7830):549–554
2. Zhou B, Ma Y, Ou P, Ye Z, Li X-Y, Vanka S, Ma T, Sun H, Wang P, Zhou P, Cooper JK, Xiao Y, Navid IA, Pan J, Song J, Mi Z (2023) Light-driven synthesis of C_2H_6 from CO_2 and H_2O on a bimetallic AuIr composite supported on InGaN nanowires. Nat Catal 6(11):987–995
3. Li X, Yu J, Jaroniec M, Chen X (2019) Cocatalysts for Selective Photoreduction of CO_2 into Solar Fuels. Chem Rev 119(6):3962–4179
4. Wang H-N, Zou Y-H, Sun H-X, Chen Y, Li S-L, Lan Y-Q (2021) Recent progress and perspectives in heterogeneous photocatalytic CO_2 reduction through a solid-gas mode. Coord Chem Rev 438:213906
5. Tian S, Yan F, Zhang Z, Jiang J (2019) Calcium-looping reforming of methane realizes in situ CO_2 utilization with improved energy efficiency. Sci Adv 5(4):eaav5077

6. Chang X, Wang T, Gong J (2016) CO_2 photo-reduction: insights into CO_2 activation and reaction on surfaces of photocatalysts. Energ Environ Sci 9(7):2177–2196
7. Monlau F, Sambusiti C, Ficara E, Aboulkas A, Barakat A, Carrère H (2015) New opportunities for agricultural digestate valorization: current situation and perspectives. Energ Environ Sci 8(9):2600–2621
8. Geng W, Xiong Y-Y, Chen C-X, Ning S, Xiong Z, Deng S, Tan Y, Song X, Pan M, Mayor M, Su C-Y (2025) Ternary metalation in a copper-covalent organic framework for tandem photocatalytic CO_2 reduction with high selectivity. Angew Chem Int Ed 64 (25), e202505546
9. Zhang J, Shi D, Yang J, Duan L, Zhang P, Gao M, He J, Gu Y, Lan K, Zhang J, Liu J, Zhao D, Ma Y (2024) One-dimensional single-crystal mesoporous TiO_2 supported CuW_6O_{24} clusters as photocatalytic cascade nanoreactor for boosting reduction of CO_2 to CH_4. Adv Mater 36(44):2409188
10. Yuan L, Qi M-Y, Tang Z-R, Xu Y-J (2021) Coupling strategy for CO_2 valorization integrated with organic synthesis by heterogeneous photocatalysis. Angew Chem Int Ed 60(39):21150–21172
11. Liu P, Huang Z, Gao X, Hong X, Zhu J, Wang G, Wu Y, Zeng J, Zheng X (2022) Synergy between palladium single atoms and nanoparticles via hydrogen spillover for enhancing CO_2 photoreduction to CH_4. Adv Mater 34 (16), e2200057
12. Wu L-W, Liu C, Han Y, Yu Y, Liu Z, Huang Y-F (2023) *In situ* spectroscopic identification of the electron-transfer intermediates of photoelectrochemical proton-coupled electron transfer of water oxidation on Au. J Am Chem Soc 145(4):2035–2039
13. Yu Z-K, Jiang M, Dai S, Zhan W, Wang Z-Q, Gong X-Q (2025) Valence restrictive metal-support interaction for boosting catalytic activity of Rh/CeO_2 in CO_2 hydrogenation. Nat Commun 16(1):9072
14. Kaishyop J, Gahtori J, Dalakoti S, Gazi MJ, Khan TS, Bordoloi A (2024) Sorption enhanced CO_2 hydrogenation to formic acid over CuZn-MOF derived catalysts. J Mater Chem A 12(14):8457–8473
15. Chen Y, Li H, Zhao W, Zhang W, Li J, Li W, Zheng X, Yan W, Zhang W, Zhu J (2019) Optimizing reaction paths for methanol synthesis from CO_2 hydrogenation *via* metal-ligand cooperativity. Nat commun 10(1):1885
16. Kumar P, Singh G, Guan X, Lee J, Bahadur R, Ramadass K, Kumar P, Kibria MG, Vidyasagar D, Yi J, Vinu A (2023) Multifunctional carbon nitride nanoarchitectures for catalysis. Chem Soc Rev 52(21):7602–7664
17. Wan L, Zhou Q, Wang X, Wood TE, Wang L, Duchesne PN, Guo J, Yan X, Xia M, Li YF, Ali FM, Ulmer U, Jia J, Li T, Sun W, Ozin GA (2019) Cu_2O nanocubes with mixed oxidation-state facets for (photo) catalytic hydrogenation of carbon dioxide. Nat Catal 2(10):889–898
18. Chen S, Qi Y, Li C, Domen K, Zhang F (2018) Surface strategies for particulate photocatalysts toward artificial photosynthesis. Joule 2(11):2260–2288
19. Li X, Yu J, Jaroniec M (2016) Hierarchical photocatalysts. Chem Soc Rev 45(9):2603–2636

20. Song S, Song H, Li L, Wang S, Chu W, Peng K, Meng X, Wang Q, Deng B, Liu Q, Wang Z, Weng Y, Hu H, Lin H, Kako T, Ye J (2021) A selective Au-ZnO/TiO_2 hybrid photocatalyst for oxidative coupling of methane to ethane with dioxygen. Nat Catal 4(12):1032–1042
21. Wagner A, Sahm CD, Reisner E (2020) Towards molecular understanding of local chemical environment effects in electro and photocatalytic CO_2 reduction. Nat Catal 3(10):775–786
22. Jiang L, Chen D, Hao Z, Cao D, Liu R, Cheng J, Chen L, Liu X, Jia B, Liu D (2024) An innovative Cu_xAg_{50-x}/UiO66-NH_2 photocatalyst prepared using a dual ship bottling strategy for photocatalytic CO_2 reduction: controlled product selectivity and pathways. Energy Environ Sci 17(21):8228–8242
23. Wu YA, McNulty I, Liu C, Lau KC, Liu Q, Paulikas AP, Sun C-J, Cai Z, Guest JR, Ren Y, Stamenkovic V, Curtiss LA, Liu Y, Rajh T (2019) Facet-dependent active sites of a single Cu_2O particle photocatalyst for CO_2 reduction to methanol. Nat Energy 4(11):957–968
24. Li X, Sun Y, Xu J, Shao Y, Wu J, Xu X, Pan Y, Ju H, Zhu J, Xie Y (2019) Selective visible-light-driven photocatalytic CO_2 reduction to CH_4 mediated by atomically thin $CuIn_5S_8$ layers. Nat Energy 4(8):690–699
25. Wang Z-S, Cui Y, Hara K, Dan-oh Y, Kasada C, Shinpo A (2007) A high-light-harvesting-efficiency coumarin dye for stable dye-sensitized solar cells. Adv Mater 19(8):1138–1141
26. Novoselov KS, Geim AK, Morozov SV, Jiang D, Zhang Y, Dubonos SV, Grigorieva IV, Firsov AA (2004) Electric field effect in atomically thin carbon films. Science 306(5696):666–669
27. Chhowalla M, Shin HS, Eda G, Li L-J, Loh KP, Zhang H (2013) The chemistry of two-dimensional layered transition metal dichalcogenide nanosheets. Nat Chem 5(4):263–275
28. Huang X, Zeng Z, Zhang H (2013) Metal dichalcogenide nanosheets: preparation, properties and applications. Chem Soc Rev 42(5):1934–1946
29. Meyer JC, Geim AK, Katsnelson MI, Novoselov KS, Booth TJ, Roth S (2007) The structure of suspended graphene sheets. Nature 446(7131):60–63
30. Butburee T, Bai Y, Wang H, Chen H, Wang Z, Liu G, Zou J, Khemthong P, Lu GQM, Wang L (2018) 2-D porous TiO_2 single-crystalline nanostructure demonstrating high photo-electrochemical water splitting performance. Adv Mater 30(21):1705666
31. Jiang X, Zhang Q, Zhao N, Li Z, Jiang L, Zhang Z (2025) 2-D Conjugated metal-organic framework-based composite membranes for nanofluidic ionic photoelectric conversion. Adv Mater 37(12):2416093
32. Rath BB, Fuchs L, Stemmler F, Rodríguez-Camargo A, Wang Y, Dorfner MFX, Olbrich J, van Slageren J, Ortmann F, Lotsch BV (2025) Insights into decoupled solar energy conversion and charge storage in a 2-D covalent organic framework for solar battery function. J Am Chem Soc 147(22):18492–18503
33. Jiao X, Chen Z, Li X, Sun Y, Gao S, Yan W, Wang C, Zhang Q, Lin Y, Luo Y, Xie Y (2017) Defect-mediated electron–hole separation in one-unit-cell $ZnIn_2S_4$ layers for boosted solar-driven CO_2 reduction. J Am Chem Soc 139(22):7586–7594

34. Kim D, Resasco J, Yu Y, Asiri AM, Yang P (2014) Synergistic geometric and electronic effects for electrochemical reduction of carbon dioxide using gold–copper bimetallic nanoparticles. Nat Commun 5(1):4948
35. Xu L, Wang Q, Gu Q, Li S, Xu Y, Chen H, Zhang H, Ye B, Chen J, Chong H, Zhou J, Liu X, Sun Z, Wei S, Yang B, Gu X-K, Wang H, Lu J (2025) Interfacial-confined oxygen vacancy clusters in ZrO_2-supported In_2O_{3-x} catalysts boost methanol production from CO_2. Angew Chem Int Ed e202508091
36. Wan X, Zhao Y, Li Y, Ma J, Gu Y, Liu C, Luo Y, Yang G, Cui Y, Liu D, Xiong Y (2025) Tailoring oxygen vacancies with atomically dispersed Cu sites for stable and efficient photothermal CO_2 conversion. Angew Chem Int Ed e202505244
37. Yao Z-C, Chai J, Tang T, Ding L, Jiang Z, Fu J, Chang X, Xu B, Zhang L, Hu J-S, Wan L-J (2025) Manipulating hydrogenation pathways enables economically viable electrocatalytic aldehyde-to-alcohol valorization. PNAS 122 (8), e2423542122
38. Zhong S, Yu D, Ma Y, Lin Y, Wang X, Yu Z, Huang M, Hou Y, Anpo M, Yu JC, Zhang J, Wang X (2025) Oxygen vacancy-enhanced selectivity in aerobic oxidation of benzene to phenol over TiO_2 photocatalysts. Angew Chem Int Ed 64 (18), e202502823
39. Ryoo R, Kim J, Jo C, Han SW, Kim J-C, Park H, Han J, Shin HS, Shin JW (2020) Rare-earth-platinum alloy nanoparticles in mesoporous zeolite for catalysis. Nature 585(7824):221–224
40. Zhao Z, Zhao Y, Lin R, Ma Y, Wang L, Liu L, Lan K, Zhang J, Chen H, Liu M, Bu F, Zhang P, Peng L, Zhang X, Liu Y, Hung C-T, Dong A, Li W, Zhao D (2022) Modular super-assembly of hierarchical superstructures from monomicelle building blocks. Sci Adv 8(19):eabo0283
41. Ling H, Sun H, Lu L, Zhang J, Liao L, Wang J, Zhang X, Lan Y, Li R, Lu W, Cai L, Bai X, Wang W (2024) Sustainable photocatalytic hydrogen peroxide production over octonary high-entropy oxide. Nat Commun 15(1):9505
42. Sun Y, Ji H, Sun Y, Zhang G, Zhou H, Cao S, Liu S, Zhang L, Li W, Zhu X, Pang H (2024) Synergistic effect of oxygen vacancy and high porosity of nano MIL-125(Ti) for enhanced photocatalytic nitrogen fixation. Angew Chem Int Ed 63 (3), e202316973
43. Lan K, Liu Y, Zhang W, Liu Y, Elzatahry A, Wang R, Xia Y, Al-Dhayan D, Zheng N, Zhao D (2018) Uniform ordered two-dimensional mesoporous TiO_2 nanosheets from hydrothermal-induced solvent-confined monomicelle assembly. J Am Chem Soc 140(11):4135–4143
44. Zhao C, Han YZ, Dai S, Chen X, Yan J, Zhang W, Su H, Lin S, Tang Z, Teo BK, Zheng N (2017) Microporous cyclic titanium-oxo clusters with labile surface ligands. Angew Chem Int Ed 56(51):16252–16256
45. Zhou M, Wang H (2022) Optimally selecting photo and electrocatalysis to facilitate CH_4 activation on TiO_2(110) surface: Localized photoexcitation versus global electric-field polarization. JACS Au 2(1):188–196
46. Li F, Wang D, Gong X-Q (2021) Subtle structure matters: boosting surface-directed photoelectron transfer via the introduction of specific monovalent oxygen vacancies in TiO_2. *PCCP 23* (35), 19854–

19861

47. Wu T, Zhao H, Zhu X, Xing Z, Liu Q, Liu T, Gao S, Lu S, Chen G, Asiri AM, Zhang Y, Sun X (2020) Identifying the origin of Ti^{3+} activity toward enhanced electrocatalytic N_2 reduction over TiO_2 nanoparticles modulated by mixed-valent copper. Adv Mater 32(30):2000299
48. Amano F, Nakata M, Yamamoto A, Tanaka T (2016) Effect of Ti^{3+} ions and conduction band electrons on photocatalytic and photoelectrochemical activity of rutile titania for water oxidation. J Phys Chem C 120(12):6467–6474
49. Powar NS, Kim S, Lee J, Gong E, Hiragond CB, Kim D, Zhang T, Kim M (2024) In, S.-I., Unravelling the effect of Ti^{3+}/Ti^{4+} active sites dynamic on reaction pathways in direct gas-solid-phase CO_2 photoreduction. *Appl. Catal. B: Environ. 352*, 124006
50. Wang Z-w, Shi Y-z, Liu C, Kang Y-y, Wu L (2022) Cu^{+}-Ti^{3+} interface interaction mediated CO_2 coordination model for controlling the selectivity of photocatalytic reduction CO_2. Appl Catal B: Environ 301:120803
51. Mercado CC, Knorr FJ, McHale JL, Usmani SM, Ichimura AS, Saraf LV (2012) Location of hole and electron traps on nanocrystalline anatase TiO_2. J Phys Chem C 116(19):10796–10804
52. Zhao B, Wang X, Zhang Y, Gao J, Chen Z, Lu Z (2019) Synergism of oxygen vacancies, Ti^{3+} and N dopants on the visible-light photocatalytic activity of N-doped TiO_2. J Photochem Photobiol A 382:111928
53. Yang S, Halliburton LE, Manivannan A, Bunton PH, Baker DB, Klemm M, Horn S, Fujishima A (2009) Photoinduced electron paramagnetic resonance study of electron traps in TiO_2 crystals: Oxygen vacancies and Ti^{3+} ions. Appl Phys Lett 94(16):162114
54. Vequizo JJM, Matsunaga H, Ishiku T, Kamimura S, Ohno T, Yamakata A (2017) Trapping-induced enhancement of photocatalytic activity on brookite TiO_2 powders: comparison with anatase and rutile TiO_2 powders. ACS Catal 7(4):2644–2651
55. Peng H, Zhuo H, Xia F, Zeng W, Sun C, Wu J (2023) Effects of bending on nucleation and injection of oxygen vacancies into the bulk lattice of Li-rich layered cathodes. Adv Funct Mater 33(51):2306804
56. Gong FQ, Liu YP, Wang Y, E W, Tian ZQ, Cheng J (2024) Machine learning molecular dynamics shows anomalous entropic effect on catalysis through surface pre-melting of nanoclusters. Angew Chem Int Ed 63 (27), e202405379

Figures

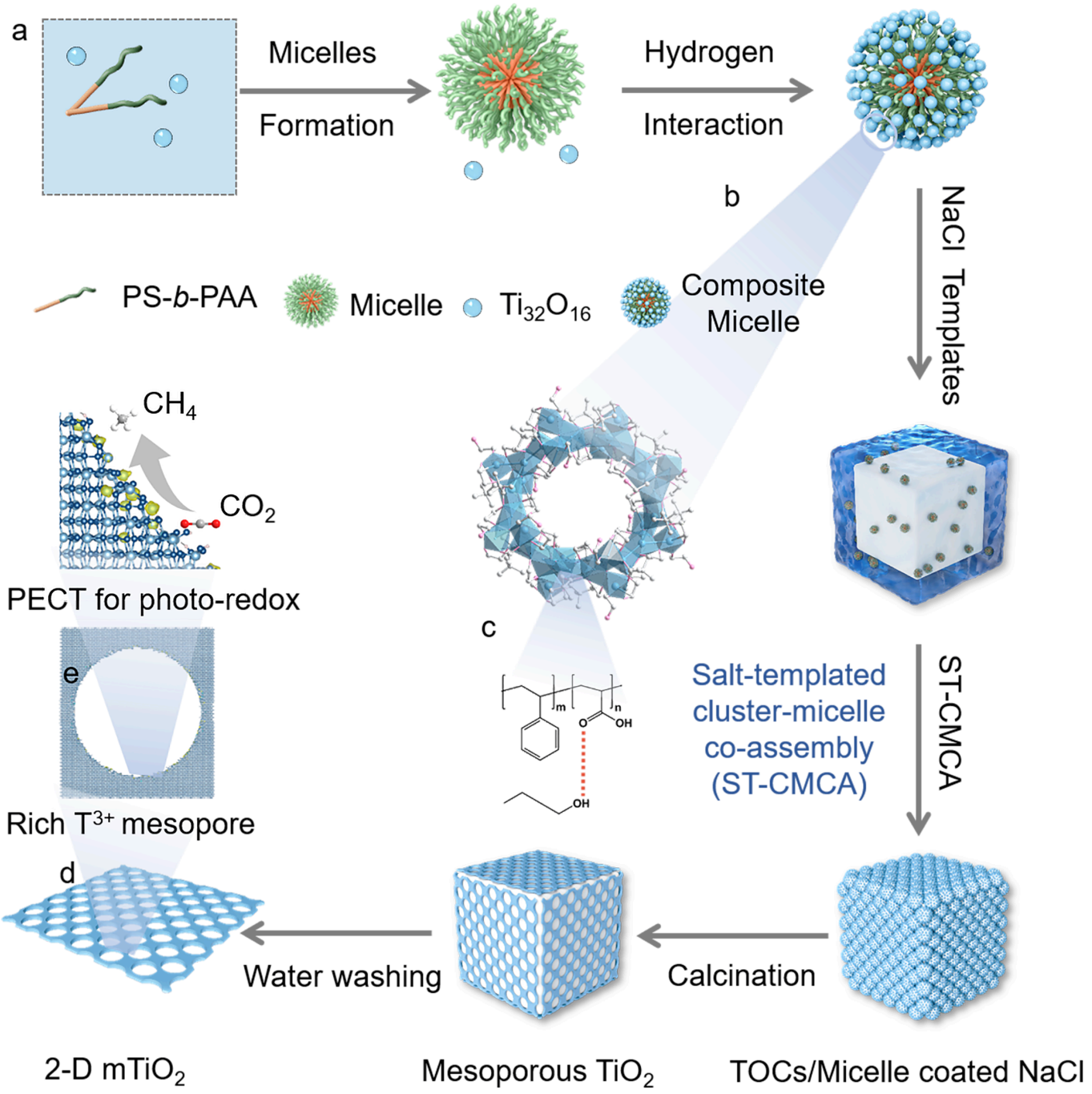


Figure 1

(a) Schematic and mechanism illustration of the formation process of the two-dimensional mesoporous TiO_2 (2-D mTiO_2) nanosheets by the salt-templated cluster-micelle co-assembly (ST-CMCA) approach, including self-assembly of nanocluster precursors $Ti_{32}O_{16}$ with diblock copolymer PS-*b*-PAA with a regularly ordered structure (such as the inverse hexagonal morphology), highly crystallized mesoporous TiO_2 under calcination process, 2-D structures were obtained by water washing; Enlargement of (b) molecular model of $Ti_{32}O_{16}$ nanocluster building units, (c) the hydrogen bonding interactin of carboxyl (PS-*b*-PAA copolymer) and ethylene glycol ligand ($Ti_{32}O_{16}$ nanocluster), (d) Ti^{3+} distribution in

mesopores, and (e) proton coupled electron transfer (PCET) for rapid photoredox of CO_2 to CH_4 in Ti^{3+} sites.

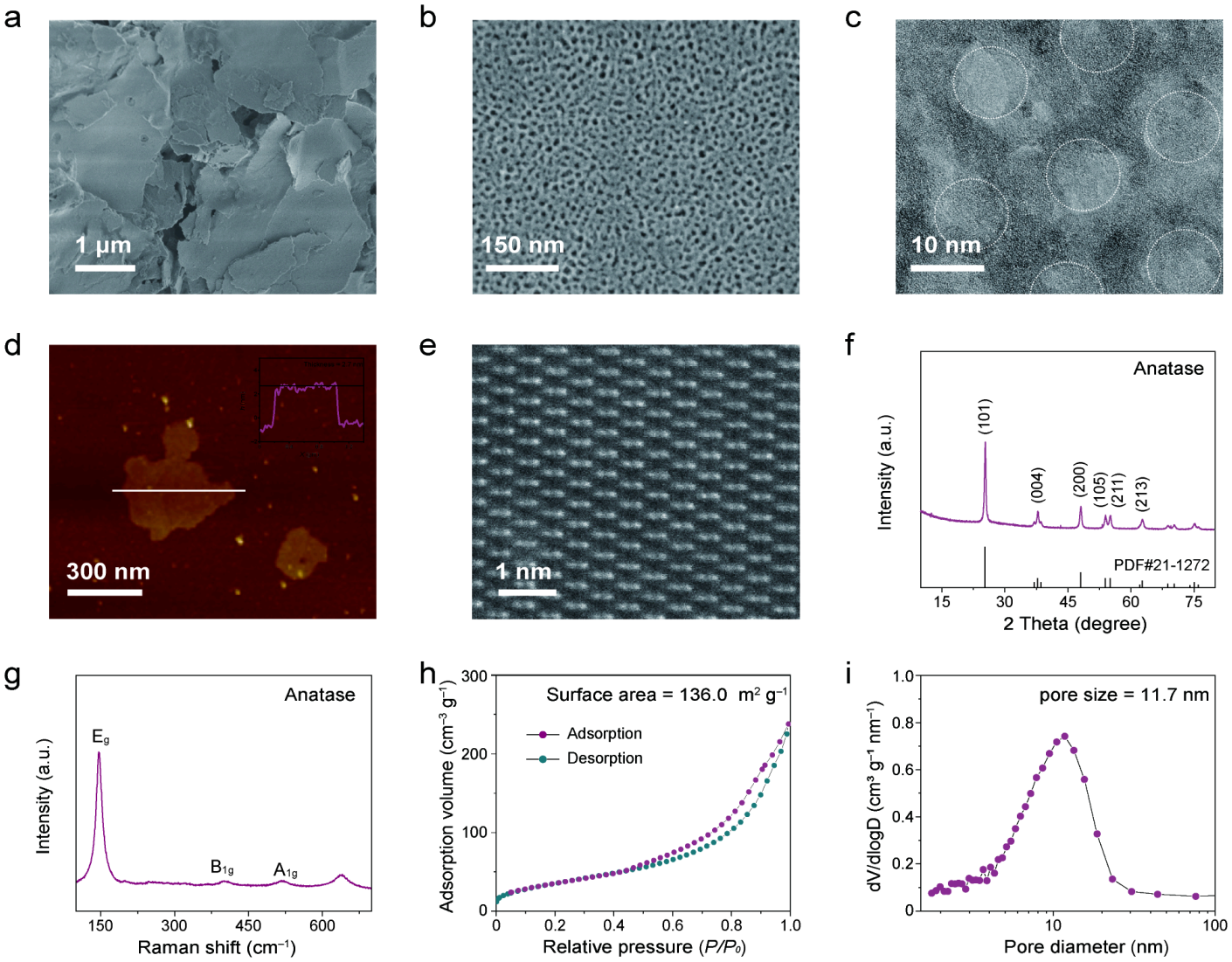


Figure 2

Structure characterizations of the 2-D mesoporous TiO_2 nanosheets (2-D mTiO_2) prepared by co-assembly of $Ti_{32}O_{16}$ nanoclusters with block copolymer PS-*b*-PAA micelle on salt NaCl crystal templates. (a) SEM image , (b) HR-SEM image, (c) TEM image, (d) AFM topography image and (inset) corresponding height information (e) AC-HAADF-STEM, (f) XRD patterns, (g) Raman spectrum, (h) Nitrogen adsorption-desorption isotherms and (i) pore-size distribution curve of 2-D mTiO_2.

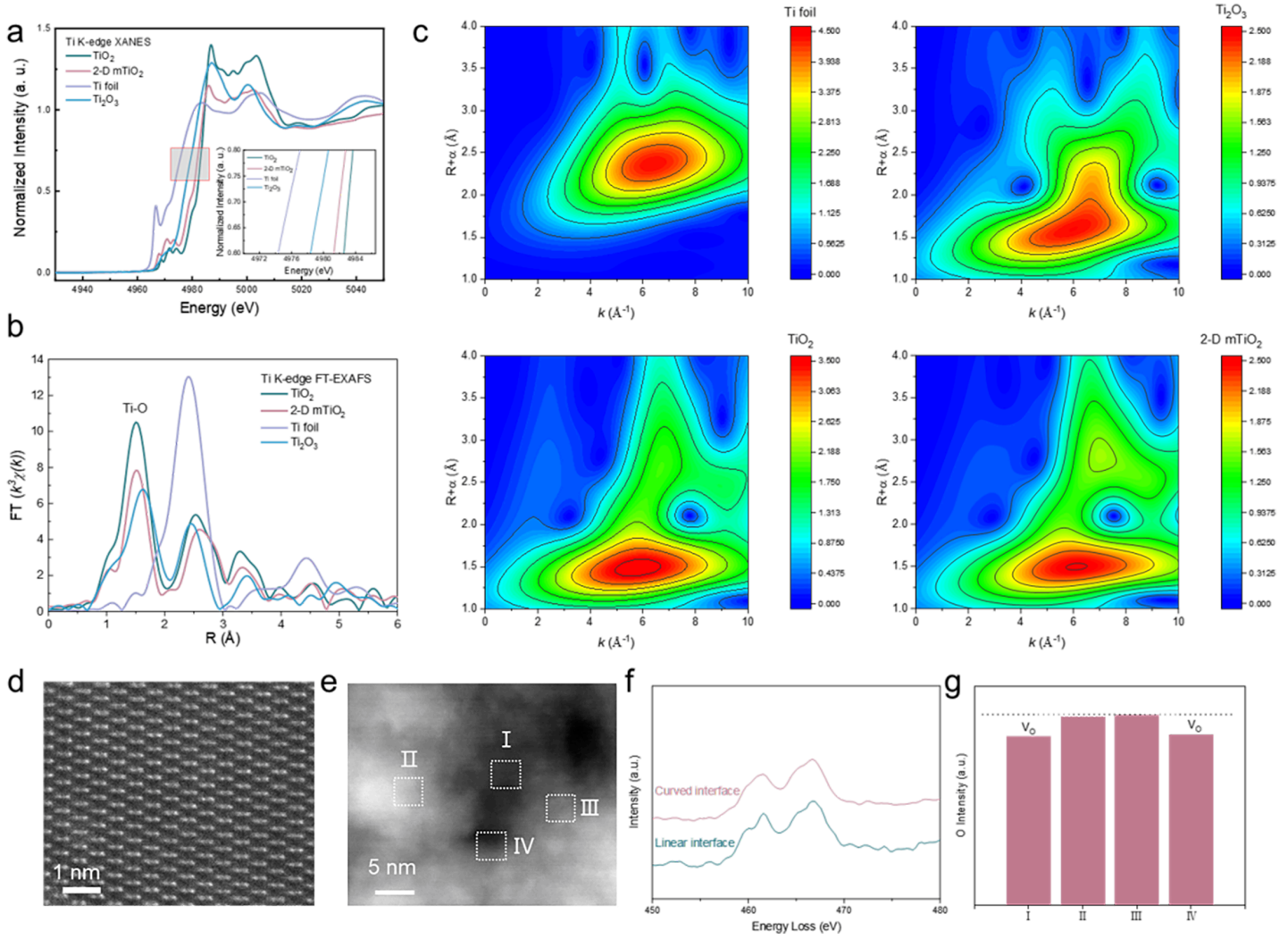


Figure 3

Characterizations of the oxygen vacancies and corresponding Ti^{3+} concentration of 2-D $mTiO_2$. (a) The XANES, (b) FT-EXAFS and (c) WT-EXAFS of Ti foil, Ti_2O_3, TiO_2 and 2-D $mTiO_2$; (d) EELS spectra of Ti L-edge at curved interface and linear interface; (e) mesoscale AC-HAADF-STEM of 2-D $mTiO_2$; (f) The normalized EELS intensity at O K-edge in selected positions (white box area in e, labeled as I, II, III, and IV). Here, we used Ti_2O_3 and Ti foil as the reference of Ti^{3+} and Ti^0, which could clearly indicate that the valence of Ti in the sample is between +3 and +4.

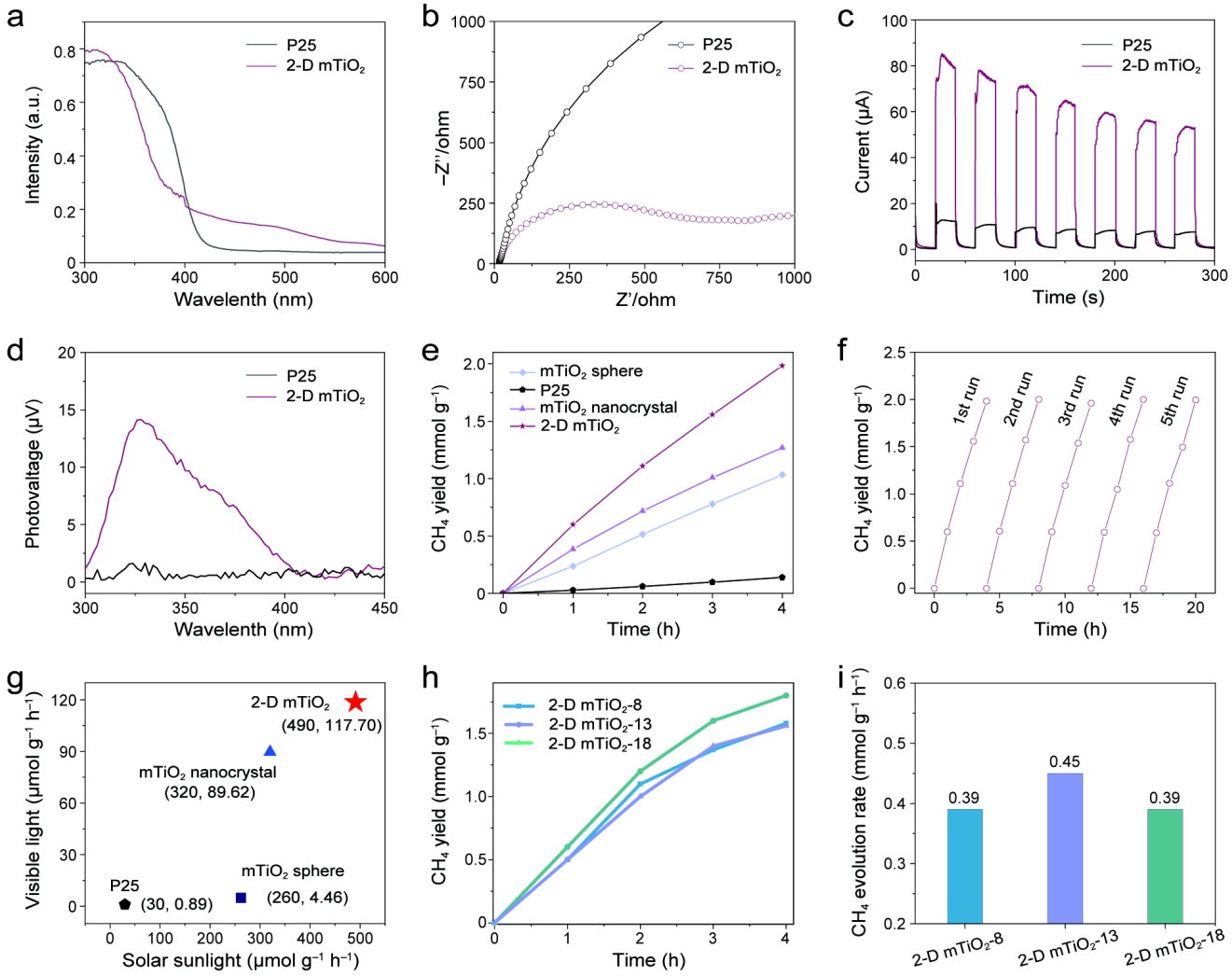


Figure 4

Photoelectrical properties of the 2-D $mTiO_2$ nanosheets. (a) Solid-state UV-vis absorption spectra, (b) EIS Nyquist plots, (c) Transient photocurrent response, (d) Surface potential voltage spectra, (e) Comparison of photocatalytic products yields (CH_4) with time under sunlight, (f) Recycling photocatalytic tests of photocatalysts, (g) Comparison of photocatalytic products yields under sunlight and visble light, (h) Comparison of photocatalytic products (CH_4) with time under sunlight of the $mTiO_2$ nanosheets with different pore sizes, (i) Comparison of photocatalytic products (CH_4) rates under sunlight of $mTiO_2$ with different pore sizes.

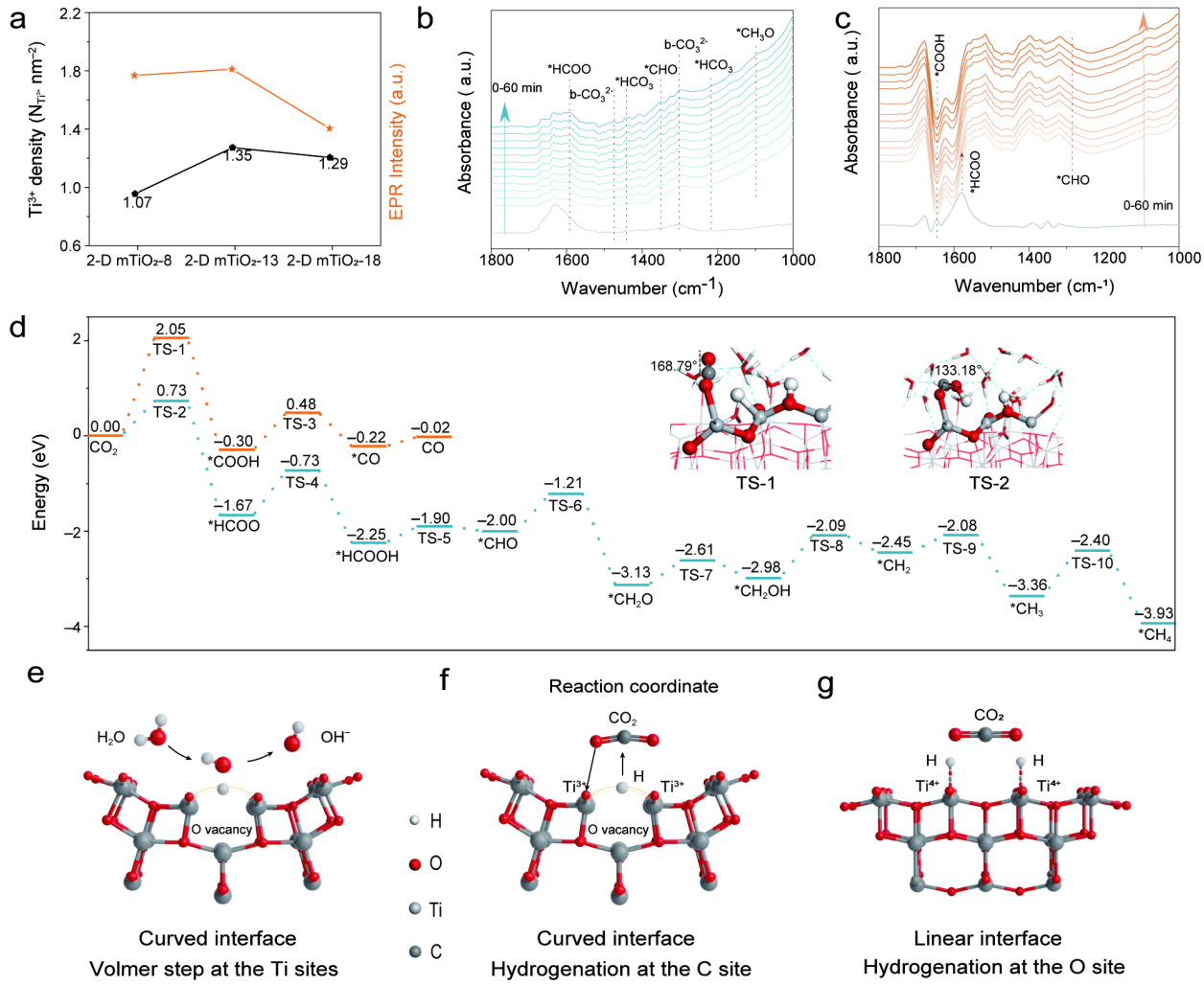


Figure 5

Mechanistic insights into enhanced photocatalytic CO_2 reduction over the 2-D mTiO_2 nanosheets. (a) Line chart of left: Ti^{3+} density from DFT calculation and right :the EPR response at *g*-value of 2.0 of 2-D mTiO_2 with different pore size. Time-resolved *In-situ* FT-IR spectra for photocatalytic CO_2 reduction on the (b) 2-D mTiO_2 nanosheets and (c) P25, (d) The free energy of the CO and CH_4 pathway produced by the catalysis on 2-D mTiO_2 nanosheets (inset: proposed mechanism for the photocatalytic CO_2 reduction), (e) transient state of TS-1 (hydrogenation at O sites) and TS-2 (hydrogenation at C sites), schematic and mechanism illustration of the hydrogenation at O sites (f) and C sites (g).

Supplementary Files

This is a list of supplementary files associated with this preprint. Click to download.

- SupportingInformation.docx
- TOC.jpg